Optimized Inversion Recovery Sequences for Quantitative T_1 and Magnetization Transfer Imaging

Ke Li,[1,2*] Zhongliang Zu,[1,2] Junzhong Xu,[1,2] Vaibhav A. Janve,[1,3] John C. Gore,[1,2,4] Mark D. Does,[1,2,4] and Daniel F. Gochberg[1–3]

Inversion recovery sequences that vary the inversion time (t_i) have been employed to determine T_1 and, more recently, quantitative magnetization transfer parameters. Specifically, in previous work, the inversion recovery pulse sequences varied t_i only while maintaining a constant delay (t_d) between repetitions. T_1 values were determined by fitting to a single exponential function, and quantitative magnetization transfer parameters were then determined by fitting to a biexponential function with an approximate solution. In the current study, new protocols are employed, which vary both t_i and t_d and fit the data with minimal approximations. Cramer-Rao lower bounds are calculated to search for acquisition schemes that will maximize the precision efficiencies of T_1 and quantitative magnetization transfer parameters. This approach is supported by Monte Carlo simulations. The optimal T_1 schemes are verified by measurements on $MnCl_2$ samples. The optimal quantitative magnetization transfer schemes are confirmed by measurements on a series of cross-linked bovine serum albumin phantoms of varying concentrations. The effects of varying the number of sampling data points are also explored, and a rapid acquisition scheme is demonstrated in vivo. These new optimized quantitative imaging methods provide an improved means for determining T_1 and magnetization transfer parameter values compared to previous inversion recovery based methods. Magn Reson Med 64:491–500, 2010. ©2010 Wiley-Liss, Inc.

Key words: quantitative magnetization transfer; T_1 measurement; inversion recovery; biexponential recovery; optimal acquisition scheme; precision efficiency

Magnetization transfer (MT), or spin exchange between protons in different tissue pools, can serve as a contrast mechanism in biologic systems. MT between free water and a broad, immobile pool of protons on macromolecules was first demonstrated by Wolff and Balaban (1), who measured the equilibrium magnetization (M_s) of water protons after applying continuous irradiation. Subsequently, Henkelman et al. (2) developed a two-pool model and performed measurements on agar gels. By varying the radiofrequency offset frequency and amplitude, they determined the relaxation and exchange rates of the two proton pools. This determination of the underlying sample parameters is referred to as quantitative magnetization transfer (qMT).

Several qMT imaging methods have been developed. Sled and Pike (3,4) extended the technique of Henkelman et al. (2) to pulsed MT, in which off-resonance saturation pulses are interleaved with on-resonance excitation pulses. Ramani et al. (5) combined the method of Sled and Pike (3,4) with an analysis similar to Henkelman et al. (2). Gloor et al. (6) developed a qMT imaging method based on balanced steady state free precession (SSFP), while Ropele et al. (7) developed a method based on stimulated echoes. Gochberg et al. (8) and Gochberg and Gore (9,10) developed a selective-inversion-recovery (SIR) technique, a qMT imaging method based on measuring the transient response to an radiofrequency pulse that selectively inverts the free water protons. MT induces biexponential recovery of longitudinal magnetization in most tissue types, including in vitro collagen (11,12), muscle (11), cartilage (13), and lung (14), and in vivo white matter (WM), gray matter (GM), and muscle (10). Prantner et al. (15) examined and dismissed non-MT explanations for this biexponential behavior in brain matter. In the most recent version of the SIR method (10), a fast-spin-echo (FSE) readout is applied, which leaves both the liquid and solid proton pools saturated and therefore facilitates determination of qMT parameters, using shorter repetition times.

The precision and accuracy of the estimates of the qMT parameters depend on several experimental factors, such as the MT pulse power (ω_1) and offset frequency (Δ) for pulsed MT and the inversion recovery time (t_i) and predelay time (t_d) values for SIR-FSE. In most published MT protocols, the set of sampling points is selected empirically. Cramer-Rao lower bounds (CRLB) (16) provide a general approach to assess this dependence on acquisition parameters by setting a lower limit on the variance of any parameter estimate based on model fitting. This method has been used to optimize acquisition schemes for T_1 measurements with constrained scan time (17), T_2 measurements (18), diffusion coefficients (19), and echo spacing for multiecho imaging (20). In Sled and Pike's pulsed-MT work (4), they used only two values of ω_1, each with a range of Δ. Based on the Ramani et al. model (5), the pulsed-MT technique was optimized by Cercignani and Alexander (21) by calculating the CRLB to obtain optimal acquisition protocols.

[1]Vanderbilt University Institute of Imaging Science, Vanderbilt University, Nashville, Tennessee, USA.
[2]Department of Radiology and Radiological Sciences, Vanderbilt University, Nashville, Tennessee, USA.
[3]Deparment of Physics and Astronomy, Vanderbilt University, Nashville, Tennessee, USA.
[4]Department of Biomedical Engineering, Vanderbilt University, Nashville, Tennessee, USA.

Grant sponsor: NIH; Grant numbers: EB001452, EB00214, EB001744, and NFS 0448915.

*Correspondence to: Ke Li, Ph.D., Vanderbilt University Institute of Imaging Science, 1161 21st Ave. S, Medical Center North, AA-1105, Nashville, TN 37232. E-mail: ke.li@vanderbilt.edu

Received 30 September 2009; revised 16 December 2009; accepted 16 February 2010.
DOI 10.1002/mrm.22440
Published online in Wiley InterScience (www.interscience.wiley.com).

For the SIR-FSE technique, Gochberg and Gore (10) used a constant t_d and varied t_i only. The experimental data were then fitted to a biexponential equation to determine first-order approximations of the qMT parameters. The current paper focuses on the optimization of this technique (10), introduces a new data analysis method as part of this optimization, and employs a new protocol that varies both t_i and t_d and fits the data with minimal approximations. CRLB are calculated to search for the variations in both t_i and t_d that will maximize the precision efficiency. The optimal schemes are supported by Monte Carlo simulations and confirmed by measurements on bovine serum albumin (BSA) phantoms. It is further demonstrated that, in practice, only five sampling points are required to determine qMT parameters and is confirmed with in vivo rat brain measurements.

SIR-FSE is essentially an inversion recovery method with the assumption of biexponential recovery due to MT. Independently varying t_i and t_d also improves the precision efficiency of simple T_1 measurements, when assuming a single exponential recovery. While this method is often replaced by the more rapid single-shot (22,23) and variable-flip-angle methods (24–26), we include a variable t_i and t_d analysis of T_1 here for its inherent interest and as an introduction to the more complex qMT case.

THEORY AND MATERIALS AND METHODS

Inversion Recovery Imaging Sequence

Conventionally, T_1 is determined by using an inversion recovery sequence (similar to Fig. 1) with $t_d \geq 5\ T_1$, during which the magnetization returns to its equilibrium state before the next sequence repetition. Previous work has optimized T_1 measurement efficiency using constant t_d or constant pulse repetition time (17). Here we will take a more general approach by varying both t_i and t_d independently without constraint. For an inversion recovery with a spin-echo or FSE readout, the measured signal is:

$$S = M_0\left[S_f(1 - e^{-t_d/T_1})e^{-t_i/T_1} + 1 - e^{-t_i/T_1}\right] \quad [1]$$

where M_0 is the magnetization of the equilibrium state, and S_f (≈ -1) quantifies the effect of the inversion pulse.

SIR-FSE qMT Imaging Sequence

The SIR-FSE pulse sequence (10) is illustrated in Fig. 1. In order to model the signal when pulse repetition time is short, an essential insight is that at the end of each repetition, both the macromolecular and free water pools have zero *z*-magnetization. The assumption has been discussed numerically and verified previously (10).

The qMT data analysis is based on a two-pool model. The coupling between the pools is modeled by adding coupling terms to the Bloch equations, as given in (9,10):

$$\begin{aligned}\frac{d}{dt}\frac{M_f(t)}{M_{f\infty}} &= -R_{1f}\left(\frac{M_f(t)}{M_{f\infty}} - 1\right) - k_{fm}\left(\frac{M_f(t)}{M_{f\infty}} - \frac{M_m(t)}{M_{m\infty}}\right),\\ \frac{d}{dt}\frac{M_m(t)}{M_{m\infty}} &= -R_{1m}\left(\frac{M_m(t)}{M_{m\infty}} - 1\right) - k_{mf}\left(\frac{M_m(t)}{M_{m\infty}} - \frac{M_f(t)}{M_{f\infty}}\right)\end{aligned} \quad [2]$$

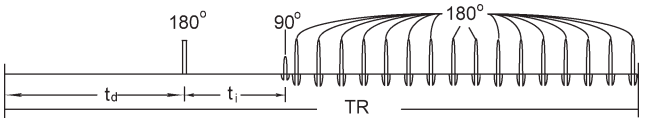

FIG. 1. The SIR-FSE pulse sequence. The quantity t_d is the predelay time and t_i is the inversion recovery time. In this work, the first eight echoes are taken for data acquisition, and the next eight echoes were taken as dummy echoes to ensure the assumption of zero Mz magnetization of both pools after the last 180° pulse. A simulation of this sequence is presented in Gochberg and Gore (10).

The subscripts f and m refer to the free and macromolecular proton pools. M_f(t) and M_m(t) are the longitudinal magnetizations at time t, whose equilibrium values are $M_f\infty$ and $M_m\infty$. R_{1f} and R_{1m} are the longitudinal relaxation rates of the free and macromolecular pools when there is no MT between them, and k_{fm} and k_{mf} are the rates of MT between them. The pool size ratio (p_m/p_f) is defined by k_{fm}/k_{mf}. The recovery of the magnetization of the free pool is described by a biexponential decay function when there are no radiofrequency pulses:

$$\frac{M_f(t)}{M_{f\infty}} = b_f^+ e^{-R_1^+ t} + b_f^- e^{-R_1^- t} + 1 \quad [3]$$

where

$$\begin{aligned}2R_1^{\pm} &= R_{1f} + R_{1m} + k_{fm} + k_{mf}\\ &\quad \pm\sqrt{(R_{1f} - R_{1m} + k_{fm} - k_{mf}) + 4k_{fm}k_{mf}}\\ b_f^{\pm} &= \pm\frac{\left[\frac{M_f(0)}{M_{f\infty}} - 1\right](R_{1f} - R_1^{\mp}) + \left[\frac{M_f(0)}{M_{f\infty}} - \frac{M_m(0)}{M_{m\infty}}\right]k_{fm}}{R_1^+ - R_1^-}\end{aligned} \quad [4]$$

where R_1^+ and R_1^- are the fast and slow recovery rates, respectively. The magnetization of the macromolecular pool is described by a biexponential equation as well, by exchanging f and m subscripts in Eqs. 3 and 4.

Applying Eqs. 3 and 4 to each free evolution period gives the signal as function of the qMT parameters, allowing us to investigate the problem and fit the qMT parameters without taking the first-order approximations utilized previously (8–10). Specifically, both pools have zero *z*-magnetization at the end of the FSE train, their magnetization at the end of t_d is written as

$$\begin{aligned}\frac{M_f(t_d^-)}{M_{f\infty}} &= -\frac{R_{1f} - R_1^-}{R_1^+ - R_1^-}e^{-R_1^+ t_d} + \frac{R_{1f} - R_1^+}{R_1^+ - R_1^-}e^{-R_1^- t_d} + 1,\\ \frac{M_m(t_d^-)}{M_{m\infty}} &= -\frac{R_{1m} - R_1^-}{R_1^+ - R_1^-}e^{-R_1^+ t_d} + \frac{R_{1m} - R_1^+}{R_1^+ - R_1^-}e^{-R_1^- t_d} + 1\end{aligned} \quad [5]$$

The effect of the inversion pulse is,

$$\begin{aligned}\frac{M_f(t_d^+)}{M_{f\infty}} &= S_f\frac{M_f(t_d^-)}{M_{f\infty}}\\ \frac{M_m(t_d^+)}{M_{m\infty}} &= S_m\frac{M_m(t_d^-)}{M_{m\infty}}\end{aligned} \quad [6]$$

where S_f and S_m are the inversion coefficients of the free and macromolecular pools, and t_d^- and t_d^+ are the time just before and after the inversion pulse, respectively.

The model discussed above contains seven parameters: R_{1f}, R_{1m}, p_m/p_f, k_{mf} (k_{fm} is equal to $k_{mf} \times p_m/p_f$), S_f, S_m, and $M_f\infty$. Among these parameters, the signal dependencies on S_m and R_{1m} are weak, as shown below. The weak dependence on R_{1m} is also the case in the pulsed saturation sequence (3–5,21). In this work, R_{1m} is set to be equal to R_{1f} for data analysis. Previous results (10) calculated an S_m of 0.83 ± 0.07 from numerical simulations, for a 1-ms hard inversion pulse on a solid pool with a Gaussian lineshape and a T_2 between 10 μs and 20 μs. There are then five remaining qMT parameters to fit: R_{1f}, p_m/p_f, k_{mf}, S_f, and $M_f\infty$. S_f is expected to be −1, but due to amplitude of static field and amplitude of radiofrequency field inhomogeneities, it has to be fit from experimental data. Finally, combining Eqs. 3–6 for each time period gives a signal function, which we use to fit the qMT parameters directly without first-order approximations.

CRLB Theory

The optimization technique presented in this work is similar to that of Cercignani and Alexander (21) but is applied to a different pulse sequence and includes acquisition time effects when calculating parameter precisions. For a set of particular qMT parameters, the CRLB derived objective function is:

$$V = \left(\sum_{j=1}^{Q} [J^{-1}]_{jj} p_j^{-2}\right) \times T_{\text{cost}}(scheme) \qquad [7]$$

where Q is the number of fitted parameters, and p_j is the j^{th} parameter. $T_{cost}(scheme)$ is given by:

$$T_{\text{cost}}(scheme) = \sum_{n=1}^{N} (t_{i,n} + t_{d,n} + t_{fse}) \qquad [8]$$

where N is the number of sampling points, t_{fse} is the length of the FSE train, and $t_{i,n}$ and $t_{d,n}$ are the nth t_i and t_d values. The Fisher information matrix J is defined by its jk^{th} element

$$J_{jk} = \frac{1}{\sigma^2} \sum_{n=1}^{N} \left(\frac{\partial S(p_1, ..., p_Q; x_n)}{\partial p_j} \frac{\partial S(p_1, \ldots, p_Q; x_n)}{\partial p_k} \right) \qquad [9]$$

where p_j is the j^{th} parameter, x are the (t_i, t_d) sampling points, and S is the signal function. The standard deviation of noise, σ, is assumed to be independent of x. As pointed out by Cercignani and Alexander (21), the essence of the term $\sum_{j=1}^{Q} [J^{-1}]_{jj} p_j^{-2}$ in Eq. 7 is $\sum \sigma_j^2 / p_j^2$, where σ_j^2 is the variance of the parameter p_j. By including the time cost term in Eq. 7, the objective function becomes essentially the inverse of precision efficiency (precision-per-unit-time (27)). The optimization process yields the maximum precision efficiency by searching for the minimum value of the objective function.

For optimization of heterogeneous samples, CRLB objective functions are constructed in a similar form as in Cercignani and Alexander (21):

$$V_{\max} = \max_{l} \left\{ \sum_{i=1}^{Q} [J_l^{-1}]_{ii} p_{il}^{-2} \right\} * T_{\text{cost}}(scheme) \qquad [10]$$

where l indexes parameter sets that characterize different tissues. Minimizing V_{max} by varying the sample points x would maximize the precision efficiency for the worst combination of parameters.

Optimization Technique

The optimization process searches for the optimal acquisition schemes, $x_1, \ldots, x_N$ that minimize V and $V_{\max}$ defined in Eqs. 7 and 10. A simulated annealing algorithm (28) was implemented in MatLab 2008b (The Mathworks, Natick, MA) to search for the optimal acquisition schemes. It evaluates 500 objective functions at each temperature T by randomly varying $x_1, \ldots, x_N$, i.e., all t_i and t_d values. The objective function is randomly perturbed by using a Metropolis et al. (29) algorithm, which allows uphill transitions and increases the possibility of reaching a global minimum. The temperature decreases according to the annealing schedule

$$T(n+1) = T(n) \times (1 - \varepsilon) \qquad [11]$$

where $0 < \varepsilon \ll 1$, until it reaches the final temperature. The initial and final temperatures are set as 100 and 0.001. To reduce the effects of local minima, the optimization is repeated from several random starting points. The scheme with a minimum objective function value is selected. The simulated annealing does not guarantee a global minimum, but we do not expect dramatic improvement in the objective function values.

By utilizing this technique, a series of optimization processes were performed. We optimized T_1 precision efficiency (using Eqs. 1 and 7–10) by varying all t_i and a single t_d values and by varying all t_i and t_d values. A set of typical parameters values is $M_f = 1$, $T_1 = 1$, and $S_f = -1$. The optimization of parameter ranges are $M_0 \in [0.5, 1.5]$, $T_1 \in [0.5, 1.5]$, and $S_f \in [-0.85, -1]$.

For qMT precision efficiency optimization, we searched for optimal acquisition schemes that have approximately the same total acquisition time as the original scheme given in Gochberg and Gore (10), by repeating the optimization process while varying the number of sampling points and then selecting the scheme that most closely matches the total acquisition time of the original. A set of typical qMT parameters (roughly those of WM) is $R_{1f} = 0.5$ Hz, $p_m/p_f = 0.10$, $k_{mf} = 30$ Hz, $S_f = -0.95$, and $M_f\infty = 1.0$, with $R_{1m} = 0.5$ Hz and $S_m = 0.83$. R_{1f} and R_{1m} values are smaller than the values presented in Gochberg and Gore (9) because the measurements in this work are performed at higher magnetic field strengths. $M_f\infty$ is simply set to 1.0 since it is only a scaling factor. The optimization of parameter ranges is $R_{1f} \in [0.4, 1.0]$, $p_m/p_f \in [0.05, 0.20]$, $k_{mf} \in (20,40)$, $S_f \in [-1.0, -0.9]$, and $M_f\infty \in [0.6, 1.5]$. This process takes more time because it has to calculate 33 parameter combination sets ($2^5 = 32$ combinations of the listed parameter values plus one set of midpoint values). The lower limits of t_i and t_d are set as 4 ms and 10 ms, respectively. These parameter ranges encompass those of the WM and GM (10), so the optimal schemes are directly applicable to in vivo brain measurements.

Imaging Methods

In the SIR-FSE sequence diagrammed in Fig. 1, we applied 16 refocusing pulses with 10-ms spacing. We

acquired data only during the first eight echoes, applying an additional eight pulses in order to ensure zero z-magnetization in both the free water and macromolecular pools at the end of the echo train. The initial inversion pulse is a 1-ms 180° hard pulse. The 90° and 180° refocusing pulses are 1-ms five-lobe sinc pulses, with time bandwidth product of 5.92 and 4.44, respectively. For each measurement, two dummy scans were applied and four or eight acquisitions were averaged, with phase cycling of the 90° and acquisition but no cycling of the initial inversion pulse (in order to destroy residual transverse magnetization). Gradient spoilers were also applied after the inversion pulse.

T_1 measurements were made on a 9.4-T Varian (Varian, Inc., Palo Alto, CA) system with a 38mm litz coil. $MnCl_2$ samples of 0.058 mM and 0.116 mM were prepared. Images were acquired with a field of view of 28 × 28mm^2, slice thickness of 2mm, and data matrix of 32 × 32. A conventional scheme, with a long t_d of 6 sec and 10 logarithmic-spaced t_i values varied between 4 ms and 6 sec, was applied, with four acquisitions averaged. In addition, eight optimized schemes were developed and applied. Four of the schemes were optimized for $M_0 = 1$, $T_1 = 1$ s, and $S_f = -1$, and four for the parameter ranges $M_0 \in [0.5, 1.5]$, $T_1 \in [0.5, 1.5]$, and $S_f \in [-0.85, -1]$. Each set of four consisted of one optimization of t_i values with a single t_d of 1 sec, and three optimizations where both t_i and t_d were allowed to vary among 10, 5, or 3 values. For ten-point optimal schemes, four acquisitions were averaged, while for five- and three-point schemes, eight acquisitions were averaged, to achieve roughly similar signal-to-noise-ratio (SNR) values for a comparison.

A series of BSA samples served as test phantoms for the qMT measurements. The BSA samples have percentage weights of 10, 15, 20, and 25, with corresponding BSA to water ratios of 0.11, 0.18, 0.25, and 0.33. An additional sample of 15% BSA with 0.05 mM $MnCl_2$ was measured as well in order to separate MT from relaxation effects. All samples were cross-linked using 25% glutaraldehyde. Measurements on these BSA samples were performed on a 4.7-T Varian system with a 63mm quad coil. Images were acquired with field of view of 40 × 40mm^2, slice thickness of 2mm, and data matrix of 64 × 64. Two sets of experiments were performed on the BSA phantoms: (1) a comparison of a previous method (10) with two optimized methods with the same acquisition time (~1 h), and (2) a comparison of two optimized methods with five and ten sampling points (and eight or four averages) with the same 16-min acquisition time. All schemes were optimized for sample parameters that roughly match WM but are also a fairly good match for BSA. A measurement of R_2 was performed as well, by using a multiple-spin-echo imaging sequence (pulse repetition time/echo time = 15,000/12 ms, 15 echoes, and four averages).

To demonstrate that the optimized schemes are applicable to brain tissues, in vivo rat brain measurements were acquired using a five-point scheme optimized for parameter ranges. The measurement was performed on a 7.0-T Varian animal system, with a 38mm litz coil. The field of view was 38 × 38mm^2, with a slice thickness of 1mm and matrix of 128 × 128. To increase SNR, eight acquisitions were averaged, giving a total time of around 32 minutes.

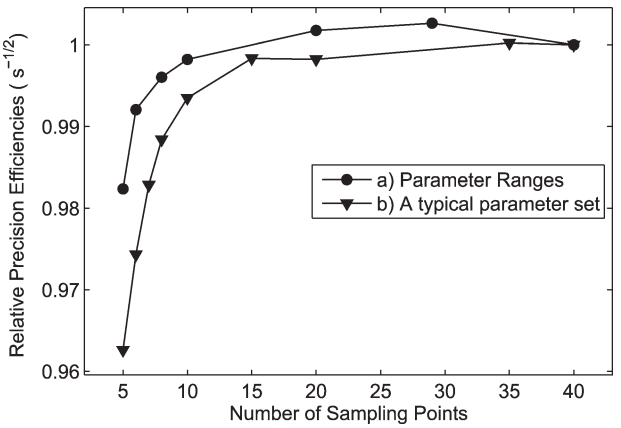

FIG. 2. Plots of relative precision efficiencies versus sampling numbers after optimizing the acquisition parameters t_i and t_d. **a:** Optimizing for parameter ranges of $R_{1f} \in [0.4, 1.0]$ Hz, $p_m/p_f \in [0.05, 0.20]$, $k_{mf} \in (20,40)$ Hz, $S_f \in [-1.0, -0.9]$, and $M_f\infty \in [0.6, 1.5]$, with precision efficiency defined by $1/\sqrt{V_{max}}$. **b:** Optimizing for a single typical parameter set: $R_{1f} = 0.5$ Hz, $p_m/p_f = 0.10$, $k_{mf} = 30$ Hz, $S_f = -0.95$, and $M_f\infty = 1.0$, with precision efficiency defined by . The efficiencies are normalized to the last data point in the two curves, respectively.

RESULTS

Optimal Schemes for Determining T_1

For a typical parameter set of $M_0 = 1$, $S_f = -1$, and $T_1 = 1$ s, and a conventional acquisition scheme, which consists of a constant t_d of 6 sec and a ten-point logarithmic spacing of t_i between 4 ms and 6 sec, the objective function value, calculated from Eqs. 1 and 7, is 286.1 sec. A ten-point scheme, which optimizes for t_i and a single t_d (1 sec), has an objective function value of 62.4 sec. The 1-sec t_d value was found to be the optimal one by comparing objective function values of optimal schemes with different t_d values. Finally, for an optimal scheme with 10 independently varied t_i and t_d values, the objective function value is 44.0 sec. There is little variation in the objective function when there are 10 (44.0 sec) or three (49.8 sec) t_i and t_d values; we plot below a similar lack of dependence on sampling point numbers in the qMT optimization case, shown in Fig. 2. Note that we have found that the minimum number of sampling points is three for T_1 determinations, with a total acquisition time of about 11 sec for one shot.

Optimal Schemes for Determining qMT Parameters

Table 1 lists three different schemes that have roughly equal acquisition times: the original scheme (column 1), the optimal scheme for typical qMT parameters (column 2), and the optimal scheme for qMT parameter ranges (column 3). For scheme 1, its objective function values are $V = 3.14 \times 10^4$ sec and $V_{max} = 7.82 \times 10^5$ sec. For scheme 2, its objective function values are $V = 1.39 \times 10^4$ sec and $V_{max} = 3.35 \times 10^5$ sec. For scheme 3, its

Table 1
Original and Optimal Schemes With Roughly the Same Total Acquisition Time

(1) Original scheme (10): V = 3.14 × 10^4 sec, Vmax = 7.82 × 10^5 sec, Time cost = 105.54 sec, t_i (sec) t_d (sec)	(2) Optimized for a typical parameter set: V = 1.39 × 10^4 sec, Vmax = 3.35 × 10^5 sec, Time cost = 105.55 sec, t_i (sec) t_d (sec)	(3) Optimized for parameter ranges: V = 1.51 × 10^4 sec, Vmax = 3.25 × 10^5 sec, Time cost = 103.25 sec, t_i (sec) t_d (sec)
0.004 3.5	0.004 1.669	0.004 2.465
0.005 3.5	0.004 1.692	0.004 2.654
0.006 3.5	0.004 1.694	0.004 2.981
0.007 3.5	0.004 1.727	0.004 4.665
0.008 3.5	0.004 1.745	0.004 4.676
0.009 3.5	0.004 4.797	0.004 4.862
0.011 3.5	0.004 4.888	0.029 4.713
0.013 3.5	0.004 4.894	0.032 3.699
0.016 3.5	0.031 4.368	0.032 4.550
0.019 3.5	0.032 2.102	0.033 4.881
0.023 3.5	0.032 4.130	0.034 5.087
0.028 3.5	0.032 4.160	0.035 3.171
0.033 3.5	0.032 4.175	0.035 3.771
0.040 3.5	0.032 4.188	0.035 3.800
0.049 3.5	0.032 4.251	0.035 3.803
0.059 3.5	0.033 2.147	0.039 2.401
0.072 3.5	0.033 2.150	0.040 1.775
0.085 3.5	0.033 2.164	0.077 1.030
0.103 3.5	0.033 2.240	0.213 2.503
0.124 3.5	0.033 2.258	0.227 2.772
0.150 3.5	0.034 2.148	0.231 2.931
0.300 3.5	0.189 2.396	0.234 3.102
1.000 3.5	0.190 2.381	0.236 2.943
2.000 3.5	0.190 2.384	0.240 3.133
10.000 3.5	0.190 2.392	0.240 3.212
	0.190 2.428	0.240 3.292
	0.191 2.362	0.252 3.271
	0.191 2.388	1.514 0.010
	0.191 2.410	2.489 0.010
	0.191 2.443	
	0.192 2.436	
	0.193 2.437	
	0.194 2.383	
	1.635 0.010	
	3.296 0.011	

objective function values are $V = 1.51 \times 10^4$ sec and $V_{max} = 3.25 \times 10^5$ sec. Note that for scheme 2, the sampling points fall into seven groups, effectively making it a seven-point sequence with variation in the SNR of each point. As for the original scheme, the objective function does not reflect the additional errors that come from the first-order approximations previously employed (9,10).

Investigation of Number of Sampling Points for qMT Measurements

As illustrated in scheme 2 in Table 1, we can determine qMT parameters with a much smaller number of sampling points. The optimization program was repeated while varying the number of sampling points, *N*. It is found that, for different *N*, the optimization processes yield similar objective function values, and only five sampling points are required to fit for five qMT parameters. In Fig. 2, plots of calculated relative precision efficiencies versus number of sampling points are shown, optimized for parameter ranges and the "typical" parameter set, respectively. Note that the precision efficiency is defined by the square root of the inverse of the CRLB objective function value, which is $1/\sqrt{V}$. The precision efficiency decreases only slightly (2% drop for the parameter ranges and 4% drop for the typical parameter set) at small *N*, meaning that there is little penalty in the fitted parameter precision efficiencies when minimizing the acquisition time by decreasing the number of acquired images, assuming one employs the optimum t_i and t_d values at each *N*.

Monte Carlo Simulations

Monte Carlo simulations were performed at different noise levels to measure the uncertainties of fitted parameters for the optimal schemes. At each noise level, 10,000 data sets were generated. Gaussian noise was introduced at each SNR level. Each data set was then

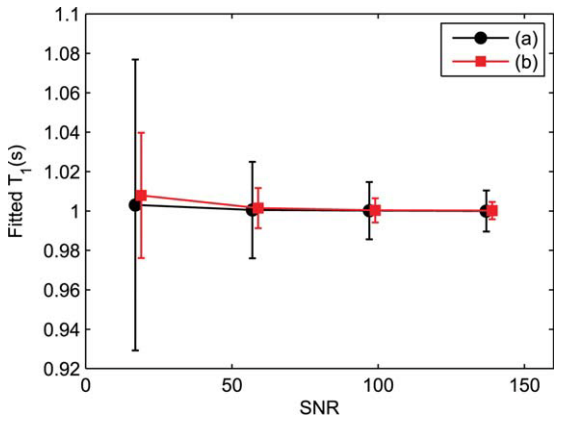

FIG. 3. Monte Carlo simulation of T_1 fitting results versus SNR using schemes: **(a)** a ten-point conventional scheme (black) with t_i logarithmically varied between 4 ms and 6 sec and t_d of 6 sec; **(b)** a three-point scheme (red) optimized for parameter values of $M_0 = 1$, $T_1 = 1$ sec, and $S_f = -1$. Data points are slightly shifted to allow a clear comparison. The uncertainties are normalized for same total acquisition time.

fitted. The mean and standard deviation of the fits define the schemes' systematic errors and uncertainties, respectively.

For T_1 simulations, the selected parameters are $M_0 = 1$, $S_f = -1$, and $T_1 = 1$. Fig. 3 shows a comparison between a conventional scheme, with ten-point logarithmic spacing of t_i between 4 ms and 6 sec, and t_d of 6 sec, and a three-point optimal scheme, with both t_i and t_d varied. Only T_1 results are shown. The optimal scheme yields much less uncertainties in T_1 values than the conventional one, with uncertainties normalized to same total acquisition time.

For qMT simulations, the selected parameters used to generate the data are $R_{1f} = 0.5$, $p_m/p_f = 0.1$, $k_{mf} = 30$, $S_f = -0.95$, and $M_f\infty = 1$. The comparison of schemes 1 and 2 is shown in Fig. 4. Scheme 3 has similar performances as scheme 2, as reflected in their objective function values, and its simulation result is not shown. $M_f\infty$ is not shown either because both schemes produce similar results. S_t is not shown either because it is not little interest. The simulation data of the original scheme 1 were processed both with and without first-order approximations. It is obvious that for the original scheme, this approximation causes systematic errors in the fitted p_m/p_f, k_{mf}, and these errors have a fractional size on the order of the pool size ratio. Schemes 1 and 2 without approximations avoid these systematic errors. Scheme 2 also produces more precise values of p_m/p_f, k_{mf} than scheme 1, especially at low SNR. Additional simulations not shown here indicate that for the worst combination of parameter sets, scheme 3 yields the least uncertainties, as reflected in its V_{max} value.

Measurements

The measured T_1 values of $MnCl_2$ samples by using different acquisition schemes are plotted in Fig. 5. The determined values and uncertainties are calculated from mean and standard deviation from pixels in the region of interest.

Fig. 6 shows corresponding plots of R_{1f}, p_m/p_f, k_{mf}, S_f, and $M_f\infty$. To show the effect of the new data processing technique, first-order approximations were employed to analyze the data acquired using scheme 1. The data from each pixel were fitted and qMT parameter values and uncertainties were set to the mean and standard deviation of the pixels in the regions of interest. The SNR of these measurements was around 270.

The comparison of measurement results using the five-point and ten-point optimal schemes is shown in Fig. 7. It shows that both schemes produce similar qMT parameters within error ranges. Similar results are obtained for the five-point and ten-point schemes optimized for parameter ranges as well.

The in vivo measurement results with the five-point scheme are show in Fig. 8. The determined qMT parameters of WM and GM are listed in Table 2.

DISCUSSION

In this paper, we have shown how to optimize the SIR-FSE sequences for T_1 and qMT imaging using CRLB

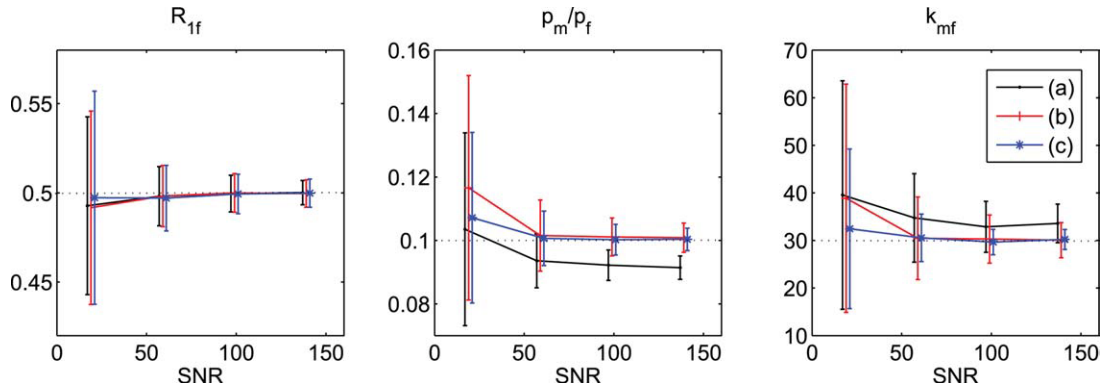

FIG. 4. Monte Carlo Simulation of qMT fitting results versus SNR: **(a)** scheme 1 (black) with first-order approximations, **(b)** scheme 1 (red) with direct fitting, and **(c)** scheme 2 (blue) with direct fitting. True values are indicated by dotted lines. Data points are slightly shifted to allow a clear comparison. Note that the previously employed first-order approximations in scheme 1 lead to systematic deviations from the input value and that scheme 2 has significantly smaller k_{mf} uncertainties than scheme 1, even when no first-order approximations are made.

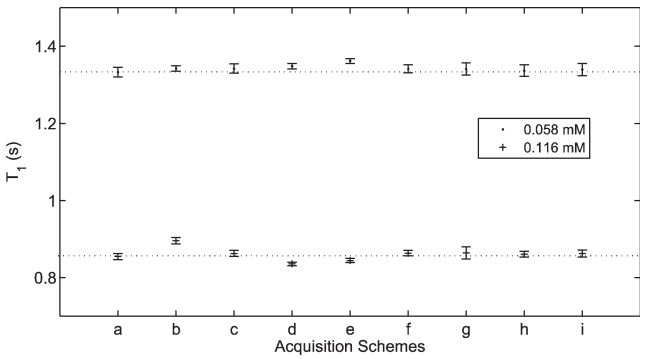

FIG. 5. Measured T_1 values of $MnCl_2$ samples of 0.058 mM and 0.116 mM by using several different acquisition schemes. **a:** A ten-point conventional scheme with t_i logarithmically varied between 4 ms and 6 sec and t_d of 6 sec. Schemes b and c are optimized by varying t_i values with a constant optimal t_d of 1 sec. Scheme b is optimized for parameter values of $M_0 = 1$, $T_1 = 1$, and $S_f = -1$. Scheme c is optimized for parameter range values of $M_0 \in [0.5, 1.5]$, $T_1 \in [0.5, 1.5]$, and $S_f \in [-0.85, -1]$. Schemes d-i are optimized by varying both t_i and t_d values. Schemes d, f, and h are optimized for a single parameter set, as in **(b)**, with numbers of sampling points of ten, five, and three, respectively. Schemes e, h, and i are optimized for parameter range values as in **(c)**, with numbers of sampling points of ten, five, and three, respectively. The determined values and uncertainties are calculated from the mean and standard deviation of the pixels in the region of interest.

methods. The original qMT technique, presented elsewhere (9,10), used fixed t_d and varied t_i only and employed first-order approximations for data fitting. According to Monte Carlo simulations, as shown in Fig. 4, first-order approximations will introduce systematic errors to p_m/p_f, k_{mf}, and S_f. The p_m/p_f values, determined by the original technique will be lower than the true value, while k_{mf} will be larger. In the new method presented here, we varied both t_d and t_i and fitted the qMT parameters with minimal approximations. Both the precision and accuracy increase, as shown in simulations and experimental results.

T_1 measurement has also been optimized using the same approach. By varying t_i and t_d independently, global optimal acquisition schemes were obtained with precision efficiencies, which are much greater than previous inversion recovery methods. This optimization is confirmed by Monte Carlo simulations, as shown in Fig. 3, by comparing a ten-point conventional scheme with a three-point optimal scheme with same total acquisition time. Fig. 5 shows a comparison of measured T_1 values between the conventional scheme and a series of optimal schemes. It is shown that the optimal schemes yield consistent T_1 values across schemes, which validates the optimization technique. It is also verified that only three sampling points are required to determine T_1 value, as shown in schemes h and i in Fig. 5. The three-point scheme optimized for parameter ranges of $M_0 \in [0.5, 1.5]$,

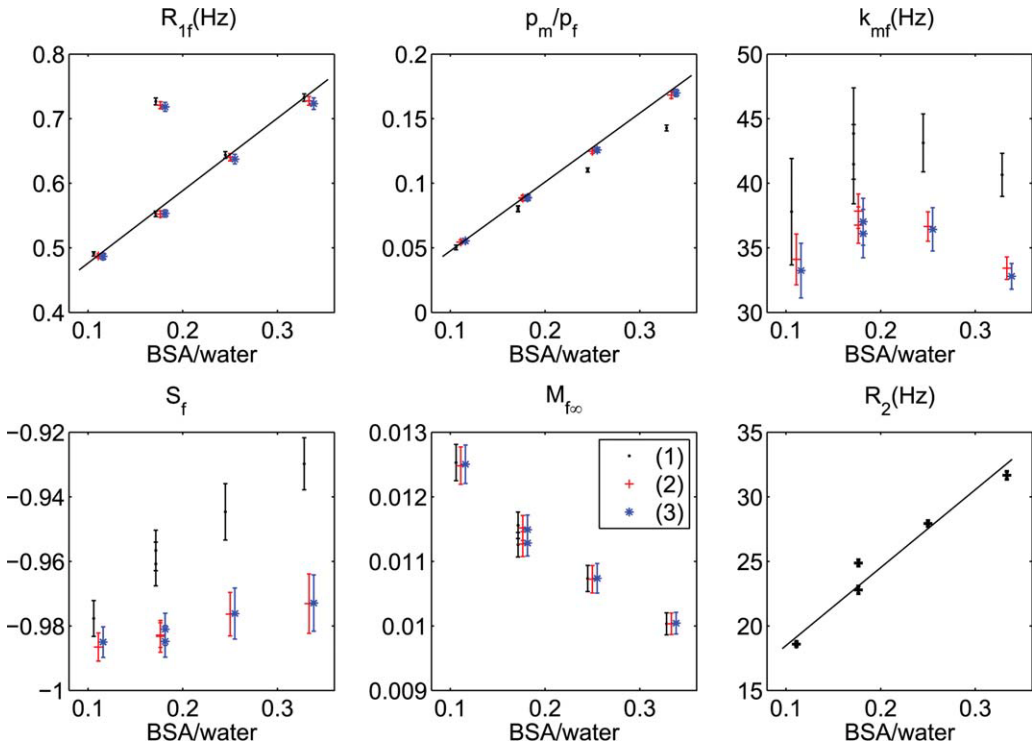

FIG. 6. Measured R_{1f}, p_m/p_f, k_{mf}, S_f, $M_f\infty$, and R_2 as a function of BSA weight versus water weight ratio using acquisition schemes 1 (black), 2 (red), and 3 (blue), where $M_f\infty$ is plotted in arbitrary units. Data points are shifted for a clear comparison. For scheme 1, first-order approximations were employed to process data. Note that the results from two 15% BSA samples are plotted, both with and without $MnCl_2$. The $MnCl_2$ changes R_{1f} and R_2 while having little effect on the fitted MT parameters, confirming that SIR-FSE is a true qMT sequence, and not just a function of the relaxation rates.

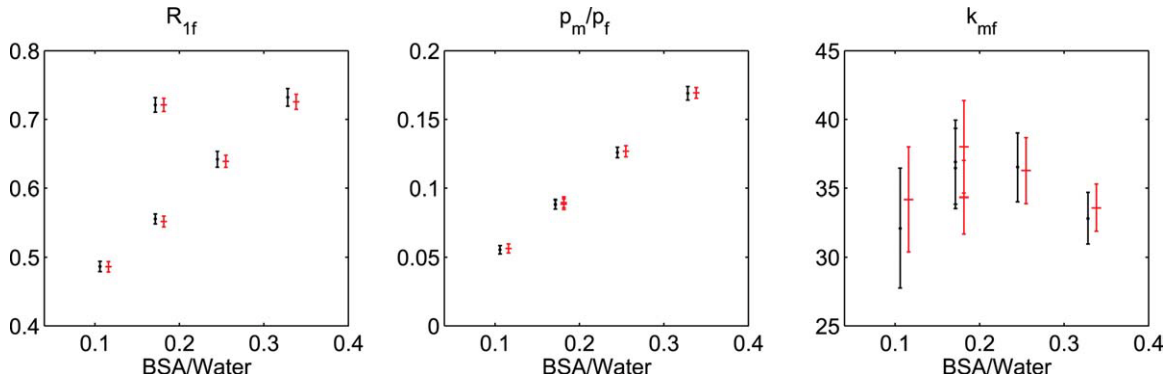

FIG. 7. A comparison of results of measuring the BSA samples by employing a five-point scheme (black) and a ten-point scheme (red) with roughly the same acquisition time. Data points are shifted for a clear comparison. While the ten-point scheme has slightly smaller parameter uncertainties, as expected from Fig. 2, there are no systematic differences in the results using the two schemes, except that the five-point scheme yielded higher M_f values due to more averages (not shown). [Color figure can be viewed in the online issue, which is available at www.interscience.wiley.com.]

$T_1 \in [0.5, 1.5]$, and $S_f \in [-0.85, -1]$, is given in Table 3, which requires about 11 sec per acquisition, so, depending on SNR requirements, an eight-shot clinical scan would take 11 sec/shot $\times$ eight shots $\times$ two averages $=$ 3 min (two averages allow phase cycling that destroys any transverse magnetization remaining after the gradient spoiling; Using a single average and fewer shots will proportionally lower the acquisition time).

The qMT optimization results were confirmed by the experimental measurements of BSA samples, as shown in Fig. 6. The optimal schemes have less uncertainty in the measured qMT parameters, most notably in k_{mf}, which, due to its greater fractional uncertainty, tends to dominate the calculation in Eq. 7. The performances of schemes 2 and 3 are similar, which is not surprising, given their similar V values in Table 1. Therefore, the optimal scheme for the set of typical parameters is applicable to a range of qMT parameters for BSA samples of different percentage weights. In other words, if the qMT parameters do not cover a very wide range, we will be able to optimize for a single parameter inside this range and apply the optimized scheme for all measurements. In addition, as in Gochberg and Gore (9), the R_{1f}, p_m/p_f values increase linearly with the BSA-to-water ratios. Note that the results from two 15% BSA samples are plotted, both with and without $MnCl_2$. The $MnCl_2$ changes R_{1f} and R_2 while having little effect on the fitted MT parameters, confirming that SIR-FSE is a true qMT sequence and not just a function of the relaxation rates.

To further confirm the optimization technique, experimental precision efficiencies were calculated. Examples are given for qMT schemes 1, 2, and 3, as listed in Table 1. The CRLB theory predicts precision efficiency ratios of 1:1.5:1.45, from their V values. Monte Carlo simulations lead to precision efficiency ratios of 1:1.56:1.50, by extracting the simulation data at an SNR of 200. The experimental precision efficiency ratios of the qMT parameters of the 15% BSA are 1:1.69:1.35. These roughly similar ratios illustrate the advantage of the optimization technique. Consistent precision efficiency ratios were obtained for $MnCl_2$ samples T_1 measurements as well. A detailed comparison of relative precision efficiencies, derived from CRLB, Monte Carlo simulations, and experimental results of T_1 and qMT, is given in Fig. 9. The experimental precision efficiencies were calculated from the 0.058-mM $MnCl_2$ and 15% BSA samples, respectively. By varying t_i and t_d simultaneously, the precision efficiencies of T_1 and qMT measurements have increased roughly 150% and 50%, respectively, compared with the conventional scheme and original technique.

Fig. 2 shows that the precision efficiency has only a weak dependence on the number of acquisitions, N. This indicates that we can take as few as five sampling points to determine the qMT parameters. This conclusion is

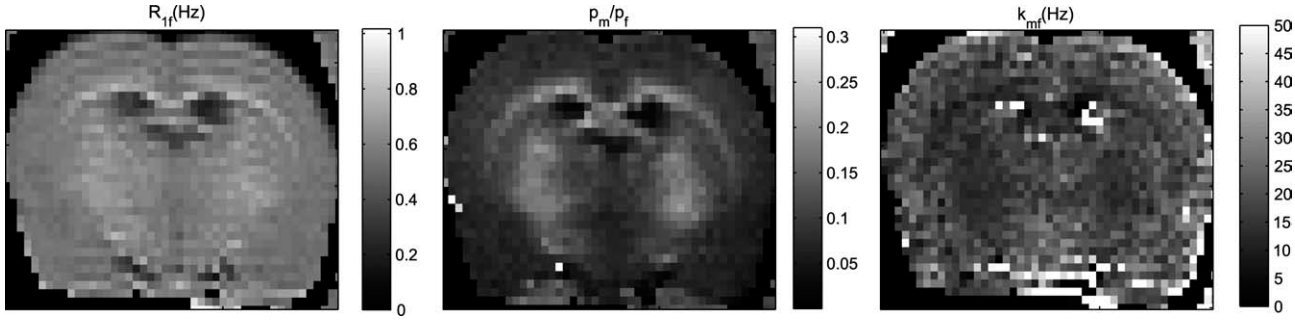

FIG. 8. Measured qMT parameter maps of a live rat with a five-point scheme, optimized for qMT parameter ranges. Images were acquired with a field of view of 38 $\times$ 38mm^2 and slice thickness of 1mm. Eight acquisitions were taken for data fitting. Note the elevated pool size ratio values due to myelin in the corpus callosum, as expected.

Table 2
Measured qMT Parameters of WM and GM in a Live Rat Brain

	R_{1f} (Hz)	p_m/p_f	k_{mf} (Hz)
WM	0.677 ± 0.076	0.173 ± 0.023	13.1 ± 2.9
GM	0.550 ± 0.046	0.080 ± 0.008	20.8 ± 6.5

confirmed by measurement of the BSA samples with five-point and ten-point schemes, as shown in Fig. 7. It is further confirmed by in vivo measurements using the five-point scheme, as shown in Fig. 8. The extracted qMT parameters of WM and GM are shown in Table 2. As shown in Monte Carlo simulations, the fitting process with first-order approximations leads to slightly larger k_{mf} but lower p_m/p_f values. This prediction is consistent with the differences between the qMT parameter values for WM in Table 2 and those in Gochberg and Gore (10).

With the verification that only a five-point scheme is required to determine the five qMT parameters, this work provides more insight in rapid qMT acquisitions. For example, a five-point optimal scheme requires about 15 sec/acquisition, so, depending on SNR requirements, an eight-shot clinical scan would take 15 sec/shot × eight shots × two averages = 4 min, making clinical application a possibility. A five-point scheme, proposed in this work for clinical applications, is shown in Table 4, which is optimized for abovementioned parameter ranges.

A related issue for clinical application is the robustness of the standard FSE implementation on a given imaging system. Any ghosting or T_2 blurring will cause correlating effects in the SIR-FSE qMT imaging sequence. Also, given the significant MT effects from the off-resonance excitation and refocusing pulses (30,31), multislice acquisitions do not make sense for SIR-FSE. However, three-dimensional acquisitions are viable, at least in a research setting, e.g., a 128 × 128 × 32 three-dimensional volume could be acquired in two averages × 15 sec/excitation × 128 × 32 phase encodes/64 echoes = 32 min, not including benefits from partial *k*-space and parallel imaging effects. This acquisition time is comparable to pulsed saturation methods (32), but without the need for separate amplitude of radiofrequency field, amplitude of static field, and T_1 maps. Pulsed saturation has, however, been more extensively tested in vivo.

In this work, we have given equal weights to all fitted parameter uncertainties in Eqs. 7 and 10. Among the five qMT parameters, the pool size ratio (p_m/p_f) is often of most interest. An alternative would be to optimize for p_m/p_f only. Optimization results, which are not shown, indicate an increase in p_m/p_f precision about 30% from such optimization, but at the cost of large systematic errors in the other qMT parameters, making it an unappealing alternative.

Fitting qMT parameters necessitates assumption about R_{1m} and S_m. We performed Monte Carlo simulations to investigate the variances of fitted qMT parameters versus different underlying R_{1m} and S_m values. We found that the fitted R_{1f}, k_{mf}, S_f, and $M_f\infty$ values are almost independent of R_{1m} and S_m. The pool size ratios, p_m/p_f, have little dependence on R_{1m} but a relatively large dependence on S_m. The simulated data were generated with $R_{1f} = 0.5$, $p_m/p_f = 0.1$, $k_{mf} = 30$, $S_f = -0.95$, and $M_f\infty = 1$, by using scheme 2 in Table 1 at an SNR of 100. For $S_m = 0.76$ and 0.9, the fitted p_m/p_f values are 0.104 ± 0.005 and 0.096 ± 0.005, respectively. With these variations, the maximum uncertainty of p_m/p_f is about 10%, which indicates that this technique is fairly robust to assumptions of R_{1m} and S_m.

Table 3
An Optimized Three-Point Scheme for Parameter Ranges of $M_0 \in [0.5, 1.5]$, $T_1 \in [0.5, 1.5]$ sec, and $S_f \in [-0.85, -1]$

t_i (sec)	0.004	0.898	4.781
t_d (sec)	1.480	3.454	0.010

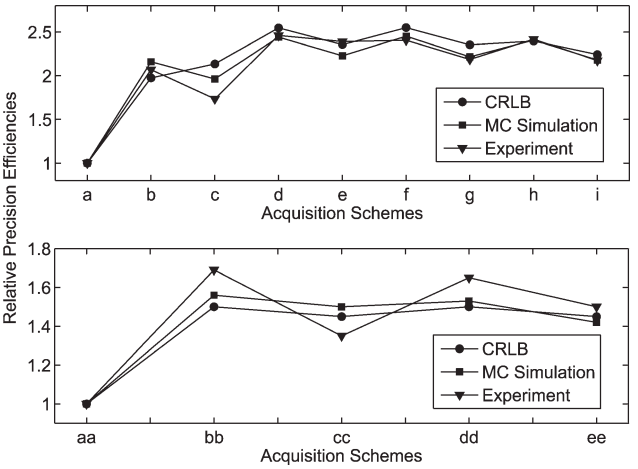

FIG. 9. Plot of relative precision efficiencies of T_1 schemes and qMT schemes for the typical parameter values listed in Fig. 2 and Fig. 3. Schemes a-i are T_1 schemes, as given in Fig. 5. Schemes aa, bb, and cc are schemes 1–3 in Table 1. Schemes dd and ee are the 10- and five-point schemes in Fig. 7. As shown in these plots, we have obtained (1) an increase in the T_1 precision efficiencies when optimizing both t_i and t_d of roughly 250% over logarithmic spacing and 25% over optimizing t_i and only a single t_d; (2) an increase in the qMT precision efficiency when optimizing both t_i and t_d of roughly 50% over the previous logarithmic spacing; and (3) only a small decrease in the precision efficiency when lowering the number of sampling points.

CONCLUSION

In conclusion, we have shown how to optimize the SIR-FSE sequences by maximizing the precision efficiency using an objective function, which includes CRLB and time cost. By varying both t_i and t_d, the precision efficiencies of both T_1 and qMT measurements are increased. Monte Carlo simulations support this approach by showing reduction in the uncertainties of fitted parameters. The optimization results are confirmed

Table 4
An Optimized Five-Point Scheme Proposed for Clinical Applications, for qMT Parameters in Ranges of $R_{1f} \in [0.4, 1.0]$ Hz, $p_m/p_f \in [0.05, 0.20]$, $k_{mf} \in [20, 40]$ Hz, $S_f \in [-1.0, -0.90]$, and $M_{f\infty} \in [0.6, 1.5]$

t_i (sec)	0.004	0.032	0.035	0.225	0.770
t_d (sec)	3.502	4.603	1.507	3.273	0.011

by measurements on $MnCl_2$ samples, BSA samples, and in vivo rat brain. Specifically, for qMT determinations, minimal approximations were applied to get rid of the systematic errors from first-order approximations in previous work (8–10). From the investigation of number of sampling data points, it is shown that five data points are enough to determine qMT parameters, and three data points are enough to determine T_1 parameters. This opens up the possibility of applying the SIR-FSE sequences to clinical two-dimensional and preclinical three-dimensional applications.

ACKNOWLEDGMENT

The authors thank Dr. Heather Whitney for assistance in BSA phantom preparation.

REFERENCES

1. Wolff SD, Balaban RS. Magnetization transfer contrast (MTC) and tissue water proton relaxation in vivo. Magn Reson Med 1989;10:135–144.
2. Henkelman RM, Huang XM, Xiang QS, Stanisz GJ, Swanson SD, Bronskill MJ. Quantitative interpretation of magnetization-transfer. Magn Reson Med 1993;29:759–766.
3. Sled JG, Pike GB. Quantitative interpretation of magnetization transfer in spoiled gradient echo MRI sequences. J Magn Reson 2000;145:24–36.
4. Sled JG, Pike GB. Quantitative imaging of magnetization transfer exchange and relaxation properties in vivo using MRI. Magn Reson Med 2001;46:923–931.
5. Ramani A, Dalton C, Miller DH, Tofts PS, Barker GJ. Precise estimate of fundamental in-vivo MT parameters in human brain in clinically feasible times. Magn Reson Imaging 2002;20:721–731.
6. Gloor M, Scheffler K, Bieri O. Quantitative magnetization transfer imaging using balanced SSFP. Magn Reson Med 2008;60:691–700.
7. Ropele S, Seifert T, Enzinger C, Fazekas F. Method for quantitative imaging of the macromolecular ^{1}H fraction in tissues. Magn Reson Med 2003;49:864–871.
8. Gochberg DF, Kennan RP, Gore JC. Quantitative studies of magnetization transfer by selective excitation and T-1 recovery. Magn Reson Med 1997;38:224–231.
9. Gochberg DF, Gore JC. Quantitative imaging of magnetization transfer using an inversion recovery sequence. Magn Reson Med 2003;49:501–505.
10. Gochberg DF, Gore JC. Quantitative magnetization transfer imaging via selective inversion recovery with short repetition times. Magn Reson Med 2007;57:437–441.
11. Edzes HT, Samulski ET. The measurement of cross-relaxation effects in the proton NMR spin-lattice relaxation of water in biological systems: hydrated collagen and muscle. J Magn Reson 1978;31:207–229.
12. Edzes HT, Samulski ET. Cross relaxation and spin diffusion in the proton NMR of hydrated collagen. Nature 1977;26:521–523.
13. Morris GA, Freemont AJ. Direct observation of the magnetization exchange dynamics responsible for magnetization transfer contrast in human cartilage in vitro. Magn Reson Med 1992;28:97–104.
14. Sobol WT, Pintar MM. NMR spectroscopy of heterogeneous solid-liquid mixtures: spin grouping and exchange analysis of proton spin relaxation in a tissue. Magn Reson Med 1987;4:537–554.
15. Prantner AM, Bretthorst GL, Neil JJ, Garbow JR, Ackerman JJ. Magnetization transfer induced biexponential longitudinal relaxation. Magn Reson Med 2008;60:555–563.
16. Kay SM. Fundamentals of statistical signal processing: estimation theory. Englewood Cliffs, NJ: Prentice-Hall; 1993.
17. Ogg RJ, Kingsley PB. Optimized precision of inversion-recovery T-1 measurements for constrained scan time. Magn Reson Med 2004;51:625–630.
18. Jones JA, Hodgkinson P, Barker AL, Hore PJ. Optimal sampling strategies for the measurement of spin-spin relaxation times. J Magn Reson B 1996;113:25–34.
19. Brihuega-Moreno O, Heese FP, Hall LD. Optimization of diffusion measurements using Cramer-Rao lower bound theory and its application to articular cartilage. Magn Reson Med 2003;50:1069–1076.
20. Dula AN, Gochberg DF, Does MD. Optimal echo spacing for multiecho imaging measurements of bi-exponential T-2 relaxation. J Magn Reson 2009;196:149–156.
21. Cercignani M, Alexander DC. Optimal acquisition schemes for in vivo quantitative magnetization transfer MRI. Magn Reson Med 2006;56:803–810.
22. Crawley AP, Henkelman RM. A comparison of one-shot and recovery methods in T1 imaging. Magn Reson Med 1988;7:23–34.
23. Look DC, Locker DR. Time saving in measurement of NMR and EPR relaxation times. Rev Sci Instrum 1970;41:250–251.
24. Wang HZ, Riederer SJ, Lee JN. Optimizing the precision in T1 relaxation estimation using limited flip angles. Magn Reson Med 1987;5:399–416.
25. Christensen KA, Grant DM, Schulman EM, Walling C. Optimal determination of relaxation-times of Fourier-transform nuclear magnetic-resonance: determination of spin-lattice relaxation-times in chemically polarized species. J Phys Chem 1974;78:1971–1977.
26. Wang J, Qiu M, Kim H, Constable RT. T1 Measurements incorporating flip angle calibration and correction in vivo. J Magn Reson 2006;182:283–292.
27. Fleysher L, Fleysher R, Liu ST, Zaaraoui W, Gonen O. Optimizing the precision-per-unit-time of quantitative MR metrics: examples for T-1, T-2, and DTI. Magn Reson Med 2007;57:380–387.
28. Kirkpatrick S, Gelatt CD, Vecchi MP. Optimization by simulated annealing. Science 1983;220:671–680.
29. Metropolis N, Rosenbluth AW, Rosenbluth MN, Tell AH. Equation of state calculations by fast computing machines. J Chem Phys 1953;21:1087.
30. Melki PS, Mulkern RV. Magnetization transfer effects in multislice RARE sequences. Magn Reson Med 1992;24:189–195.
31. Dixon WT, Engels H, Castillo M, Sardashti M. Incidental magnetization transfer contrast in standard multislice imaging. Magn Reson Imaging 1990;8:417–422.
32. Cercignani M, Symms MR, Schmierer K, Boulby PA, Tozer DJ, Ron M, Tofts PS, Barker GJ. Three-dimensional quantitative magnetisation transfer imaging of the human brain. Neuroimage 2005;27:436–441.